

Increased H₂CO production in the outer disk around HD 163296

M.T. Carney¹, M.R. Hogerheijde¹, R.A. Loomis², V.N. Salinas¹, K.I. Öberg², C. Qi², D.J. Wilner²

¹ Leiden Observatory, Leiden University, PO Box 9513, 2300 RA, The Netherlands.
e-mail: masoncarney@strw.leidenuniv.nl

² Department of Astronomy, Harvard University, Cambridge, MA 02138, USA

Received July 19, 2016 / Accepted May 25, 2017

ABSTRACT

Context. The gas and dust in circumstellar disks provide the raw materials to form planets. The study of organic molecules and their building blocks in such disks offers insight into the origin of the prebiotic environment of terrestrial planets.

Aims. We aim to determine the distribution of formaldehyde, H₂CO, in the disk around HD 163296 to assess the contribution of gas- and solid-phase formation routes of this simple organic.

Methods. Three formaldehyde lines were observed (H₂CO 3₀₃–2₀₂, H₂CO 3₂₂–2₂₁, and H₂CO 3₂₁–2₂₀) in the protoplanetary disk around the Herbig Ae star HD 163296 with ALMA at ~0.5'' (60 AU) spatial resolution. Different parameterizations of the H₂CO abundance were compared to the observed visibilities, using either a characteristic temperature, a characteristic radius or a radial power law index to describe the H₂CO chemistry. Similar models were applied to ALMA Science Verification data of C¹⁸O. χ^2 minimization on the visibilities was used to determine the best-fit model in each scenario.

Results. H₂CO 3₀₃–2₀₂ was readily detected via imaging, while the weaker H₂CO 3₂₂–2₂₁ and H₂CO 3₂₁–2₂₀ lines required matched filter analysis to detect. H₂CO is present throughout most of the gaseous disk, extending out to ~550 AU. An apparent 50 AU inner radius of the H₂CO emission is likely caused by an optically thick dust continuum. The H₂CO radial intensity profile shows a peak at ~100 AU and a secondary bump at ~300 AU, suggesting increased production in the outer disk. In all modeling scenarios, fits to the H₂CO data show an increased abundance in the outer disk. The overall best-fit H₂CO model shows a factor of two enhancement beyond a radius of 270±20 AU, with an inner abundance (relative to H₂) of 2–5 × 10⁻¹². The H₂CO emitting region has a lower limit on the kinetic temperature of $T > 20$ K. The C¹⁸O modeling suggests an order of magnitude depletion of C¹⁸O in the outer disk and an abundance of 4–12 × 10⁻⁸ in the inner disk.

Conclusions. There is a desorption front seen in the H₂CO emission that roughly coincides with the outer edge of the 1.3 millimeter continuum. The increase in H₂CO outer disk emission could be a result of hydrogenation of CO ices on dust grains that are then sublimated via thermal desorption or UV photodesorption, or more efficient gas-phase production beyond ~300 AU if CO is photodissociated in this region.

Key words. astrochemistry – protoplanetary disks – submillimeter:stars

1. Introduction

Protoplanetary disks have a layered temperature and density structure that results in a cold, dense midplane where gaseous molecules freeze out onto icy mantles around small dust grains. Chemical reactions and radiative processing of atoms and molecules locked up in ices can create organic molecules of increasing complexity (Watanabe et al. 2003; Öberg et al. 2009, 2010a; Herbst & van Dishoeck 2009). The high densities and the vertical settling of larger grains make the disk midplane an ideal site for grain growth and the formation of comets and planetesimals (Dullemond & Dominik 2005; Andrews & Williams 2005; D’Alessio et al. 2006). The cold, complex molecular reservoir may be incorporated into small icy bodies in the midplane and remain relatively unprocessed, thus comets may preserve the chemical composition of the disk at the time of their formation (van Dishoeck & Blake 1998; Mumma & Charnley 2011). Comets and other planetesimals are possible delivery mechanisms of organics to terrestrial bodies during the early stages of the solar system, thus it is important to understand the chemistry and composition of their natal environments. Observations of molecular emission lines can determine the distribution and abundance of a molecular species and constrain its location in a protoplanetary disk. Characterizing simple organic molecules

that may be produced in the disk midplane, such as H₂CO, can constrain available formation scenarios for complex organic molecules (COMs). H₂CO acts as a precursor to CH₃OH, which is an important building block for other COMs (Öberg et al. 2009; Walsh et al. 2014). Thus, determining the dominant formation mechanism for H₂CO and its distribution in disks can help to constrain abundances for CH₃OH and the complex organic reservoir.

A major formation pathway of H₂CO is expected to be the hydrogenation of CO ices in the cold midplane of the disk (Watanabe et al. 2003; Cuppen et al. 2009). H₂CO also has a gas-phase formation route via neutral-neutral reactions of CH₃ and O at higher (≥ 200 K) temperatures (Fockenberg & Preses 2002; Atkinson et al. 2006). Formaldehyde has already been detected toward several protoplanetary disks (Aikawa et al. 2003; Öberg et al. 2010b; Qi et al. 2013; van der Marel et al. 2014; Loomis et al. 2015, Öberg et al. in press), but it is difficult to determine the contribution of H₂CO formed in the gas phase versus that formed via surface reactions. It is important to consider the distribution of H₂CO in relation to the freeze-out of CO, i.e. the CO snow line. H₂CO that exists well beyond the CO snow line is likely formed on the icy mantles of dust grains while H₂CO

Table 1: HD 163296 Observational Parameters

Project 2013.1.01268.S			
Dates Observed	2014 July 27, 28, 29		
Baselines	21 – 795 m 16 – 598 k λ		
	H ₂ CO 3 ₀₃ –2 ₀₂	H ₂ CO 3 ₂₂ –2 ₂₁	H ₂ CO 3 ₂₁ –2 ₂₀
Rest frequency [GHz]	218.222	218.476	218.760
Synthesized beam [FWHM]	0.54'' \times 0.42''	0.54'' \times 0.42''	0.53'' \times 0.42''
Position angle	89.3°	86.6°	87.9°
Channel width [km s ⁻¹]	0.084	0.084	0.084
rms noise ^a [mJy beam ⁻¹]	1.8	2.6	2.6
Integrated flux [Jy km s ⁻¹]	0.64 \pm 0.06 ^b	>0.036, <0.27 ^c	>0.032, <0.31 ^c
Weighting	natural	natural	natural
Continuum Frequency [GHz]	225.0		
Synthesized beam [FWHM]	0.42'' \times 0.33''		
Position angle	77.5°		
rms noise [mJy beam ⁻¹]	0.05		
Integrated flux [mJy]	652 \pm 65		
Weighting	Briggs, robust = 0.5		
Project 2011.1.00010.SV			
Dates Observed	2012 June 09, 23, July 07		
Baselines	21 – 536 m 16 – 402 k λ		
	C ¹⁸ O 2–1		
Rest frequency [GHz]	219.560		
Synthesized beam [FWHM]	0.87'' \times 0.71''		
Position angle	64.0°		
Channel width [km s ⁻¹]	0.334		
rms noise ^a [mJy beam ⁻¹]	4.2		
Integrated flux ^d [Jy km s ⁻¹]	7.4 \pm 0.7		
Weighting	natural		

Notes. Flux errors are dominated by systematic uncertainties, taken to be $\sim 10\%$. ^(a) Noise values are per image channel. ^(b) Line flux derived from spatial and spectral integration after masking pixels with $<3\sigma$ emission. ^(c) Line flux lower limit derived from the peak σ -ratio based on matched-filter detections. Upper limits are $3\sigma_1$ where σ_1 is defined in Section 3.1. ^(d) Line flux derived from spatial and spectral integration over a 5.6'' aperture and velocity channels 0.87 km s⁻¹ – 12.1 km s⁻¹.

located within the CO snow line forms via gas-phase pathways at higher temperatures.

Qi et al. (2013) attempted to reproduce Submillimeter Array (SMA) observations of H₂CO around TW Hya and HD 163296 with two simple parameterized models: a power-law H₂CO column density with an inner radius and a ring-like H₂CO distribution with an upper boundary set by the CO freeze-out temperature. They found that both models indicated H₂CO is produced mostly at larger radii beyond the CO snow line in the disk around HD 163296, consistent with a scenario where formaldehyde forms in CO ice and is subsequently released back into the gas phase. Loomis et al. (2015) modeled H₂CO in DM Tau observed with the Atacama Large Millimeter/submillimeter Array (ALMA) using a small chemical network with and without grain-surface formation. They found that both gas- and solid-phase production of H₂CO were needed to reproduce the centrally peaked emission and the emission exterior to the CO snow line in DM Tau.

HD 163296 (MWC 275) is an ideal testbed for chemical processing in protoplanetary disks, in particular for organics. It is an isolated Herbig Ae protostar with spectral type A2Ve, an age of approximately 5 Myr, located at 122 pc (de Gregorio-Monsalvo et al. 2013). The protostar is surrounded by a large gas-rich protoplanetary disk that extends to ~ 550 AU (Isella et al. 2007) with stellar mass $M_* = 2.3 M_\odot$, disk mass $M_{\text{disk}} = 0.089 M_\odot$, and an inclination of 44° based on the Qi et al. (2011) physical model. At such an inclination, vertical structure as well as radial struc-

ture can be inferred from molecular line emission. The proximity and size of the disk combined with the strong UV field of the Herbig Ae protostar provides a unique opportunity to fully resolve the location of the CO snow line around HD 163296. Several attempts have already been made to constrain the location of the CO snow line in this disk (Qi et al. 2011; Mathews et al. 2013; Qi et al. 2015). Current estimates by Qi et al. (2015) place CO freeze-out at 90 AU, corresponding to ~ 24 K in this disk. HD 163296 is one of the best candidates to probe the formation of organics with respect to the freeze-out of abundant volatiles like CO. Observations of H₂CO in combination with tracers of the CO snow line, such as the optically thin C¹⁸O isotopologue, DCO⁺, or N₂H⁺, provide insight into the formation of organic molecules in Herbig Ae/Be disks.

This paper presents ALMA observations of H₂CO toward HD 163296 and characterizes its distribution throughout the disk. Our analysis also makes use of C¹⁸O Science Verification data, which has been previously reported (Rosenfeld et al. 2013; Qi et al. 2015). Section 2 describes the observations and data reduction. The detection of H₂CO, the modeling of H₂CO and C¹⁸O distributions and abundances, and the calculation of excitation temperatures for H₂CO are discussed in Section 3. In Section 4 we discuss the relationship between H₂CO, C¹⁸O, and the millimeter continuum, and the implications for H₂CO formation.

2. Observations and Reduction

HD 163296 (J2000: R.A. = 17^h56^m21.280^s, DEC = -21°57′22.441″) was observed on 2014 July 27, 28, and 29 with ALMA in band 6 as part of Cycle 2. In total 33 antennas were used in the C34 configuration to achieve a resolution of $\sim 0.4''$. Band 6 operates in the 211–275 GHz range as a 2SB receiver. The upper sideband contained continuum observations in the Time Domain Mode (TDM) correlator setting with 128 channels over a 2 GHz bandwidth centered at 233 GHz, presented in Zhang et al. (2016). Three transitions of H₂CO were observed in the lower sideband with the Frequency Domain Mode (FDM) correlator setting: H₂CO 3₀₃–2₀₂ at 218.22219 GHz, H₂CO 3₂₂–2₂₁ at 218.475632 GHz, and H₂CO 3₂₁–2₂₀ at 218.760066 GHz. Each line had a bandwidth of 56.6 MHz with 960 channels, providing a frequency (velocity) resolution of 0.061 MHz (0.084 km s⁻¹). Table 1 summarizes the observational parameters of each line. Three additional lines, DCO⁺ 3–2 at 216.11258 GHz, DCN 3–2 at 217.23853 GHz, and N₂D⁺ 3–2 at 231.321828 GHz were also observed with the same spectral parameters and will be presented in Salinas et al. (in prep).

Visibility data were obtained over four execution blocks of ~ 30 minutes (x1) and ~ 90 minutes (x3) at 6.05 seconds per integration for 155 minutes total time on source. System temperatures varied from 50–150 K. The average precipitable water vapor across all observations was 1.0 mm. The Common Astronomy Software Applications (CASA) package was used to calibrate the data with an automated script provided by the ALMA staff. Calibration of each execution block was done with J1700-2610 as the delay calibrator, J1733-1304 as the bandpass and gain calibrator, J1733-1304 as the flux calibrator for three out of four blocks, and Titan as the flux calibrator for the final block. After initial calibration of individual execution blocks, gain calibration solutions obtained from models of Titan were used to derive fluxes for J1733-1304, which was then used as the flux calibrator in all spectral windows and all execution blocks for consistency. Amplitudes for HD 163296 were rescaled across all blocks using J1733-1304 as the flux calibrator. The average flux values for J1733-1304 were 1.329 Jy in the lower sideband and 1.255 Jy in the upper sideband. The total flux for HD 163296 was found to be within 5% across all execution blocks. All measurement sets were subsequently concatenated and time binned to 30s integration time per visibility for imaging and analysis.

Self-calibration for HD 163296 was performed using the continuum TDM spectral window and all line-free channels of the FDM spectral windows. DV11 was chosen as the reference antenna. A minimum of four baselines per antenna and a minimum signal-to-noise ratio (SNR) of two were required. Calibration solutions were calculated twice for phase and once for amplitude. The first phase solution interval (solint) was 500s, the second phase and amplitude solutions had solint equal to the binned integration time (30s). Continuum subtraction of the line data was done in the uv plane using a single-order polynomial fit to the line-free channels. CLEAN imaging was done with natural weighting for each continuum-subtracted H₂CO line down to a threshold of 4 mJy.

This work also uses C¹⁸O 2–1 calibrated data of HD 163296 from the ALMA project 2011.0.00010.SV obtained from the publicly available ALMA Science Verification Data website.¹ See Rosenfeld et al. (2013) for details on the calibration of the data set. The flux for the C¹⁸O 2–1 line (Table 1) is consistent with previously reported values (Rosenfeld et al. 2013; Qi et al.

¹ <https://almascience.nrao.edu/alma-data/science-verification>

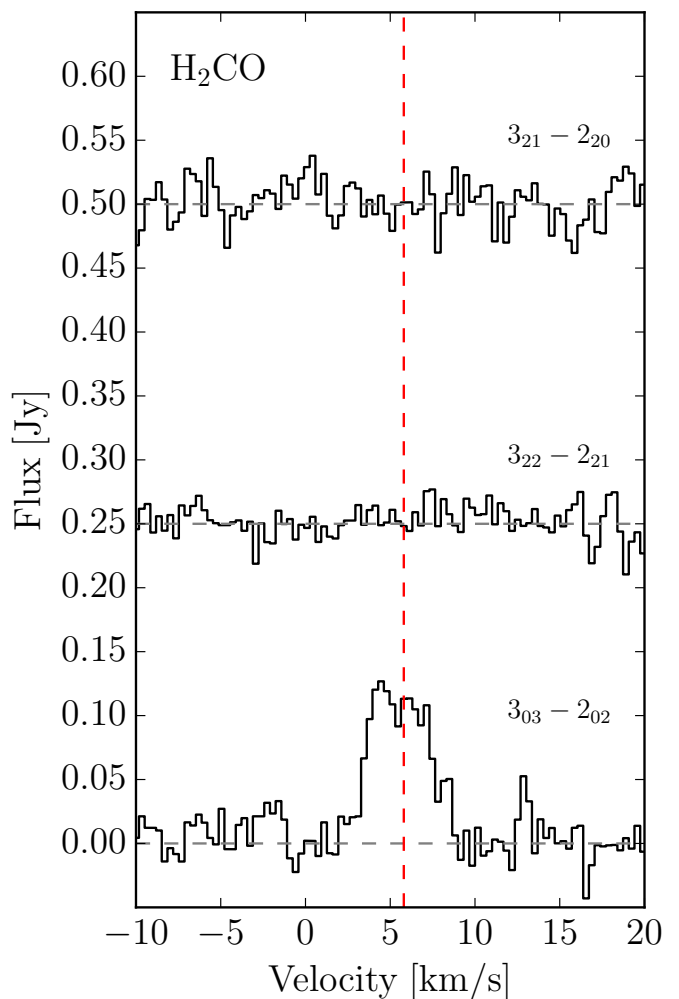


Fig. 1: Disk-integrated H₂CO spectra using a 5.6'' circular aperture. H₂CO 3₀₃–2₀₂, H₂CO 3₂₂–2₂₁, and H₂CO 3₂₁–2₂₀ are at y-offsets of 0, 0.25, and 0.5 Jy, respectively, shown in dashed gray lines. The vertical dashed red line shows the systemic velocity. The spectra are Hanning smoothed to 0.336 km s⁻¹ channels.

2015). The following software and coding languages were used for data analysis in this paper: the CASA package (McMullin et al. 2007), the MIRIAD package (Sault et al. 1995), and PYTHON.

3. Results

The following sections present results of H₂CO observations in the disk around HD 163296. Physical parameters of the lines and their distribution throughout the disk are discussed in Section 3.1. Models of H₂CO and C¹⁸O emission and their abundances are presented in Section 3.2. Constraints on the excitation temperature of H₂CO are discussed in Section 3.3.

3.1. Detection and distribution of H₂CO

The spatially integrated spectrum for each H₂CO line can be found in Figure 1. The 3₀₃–2₀₂ transition is readily detected in the spectrum extracted from CLEAN imaging. The two weaker lines are not detected in the extracted spectra, but when applying a matched-filter technique (see Sec 3.1.1), the lines are clearly detected and can be used to provide constraints on the H₂CO ex-

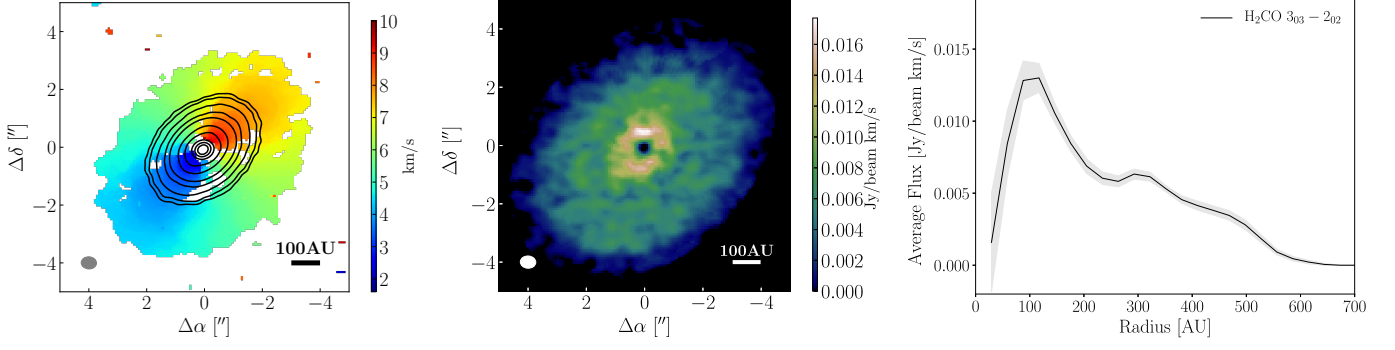


Fig. 2: Moment maps and radial profile of $\text{H}_2\text{CO } 3_{03}-2_{02}$. (*Left*) Moment 1 map from $0.76 - 10.84 \text{ km s}^{-1}$, clipped at 3σ . Solid black contours show the $225 \text{ GHz}/1.3 \text{ mm}$ emission at $5.0 \times 10^{-5} (1\sigma) \times [5, 10, 25, 50, 100, 300, 500, 1000, 1500, 2000] \text{ Jy beam}^{-1}$. Synthesized beam and AU scale are shown in the lower corners. (*Center*) Moment 0 map integrated over $0.76 - 10.84 \text{ km s}^{-1}$ after applying a Keplerian mask. Synthesized beam and AU scale are shown in the lower corners. (*Right*) Radial intensity curve from azimuthally-averaged elliptical annuli projected to $i=44^\circ$, $\text{P.A.}=133^\circ$. Shaded gray area represents 1σ errors.

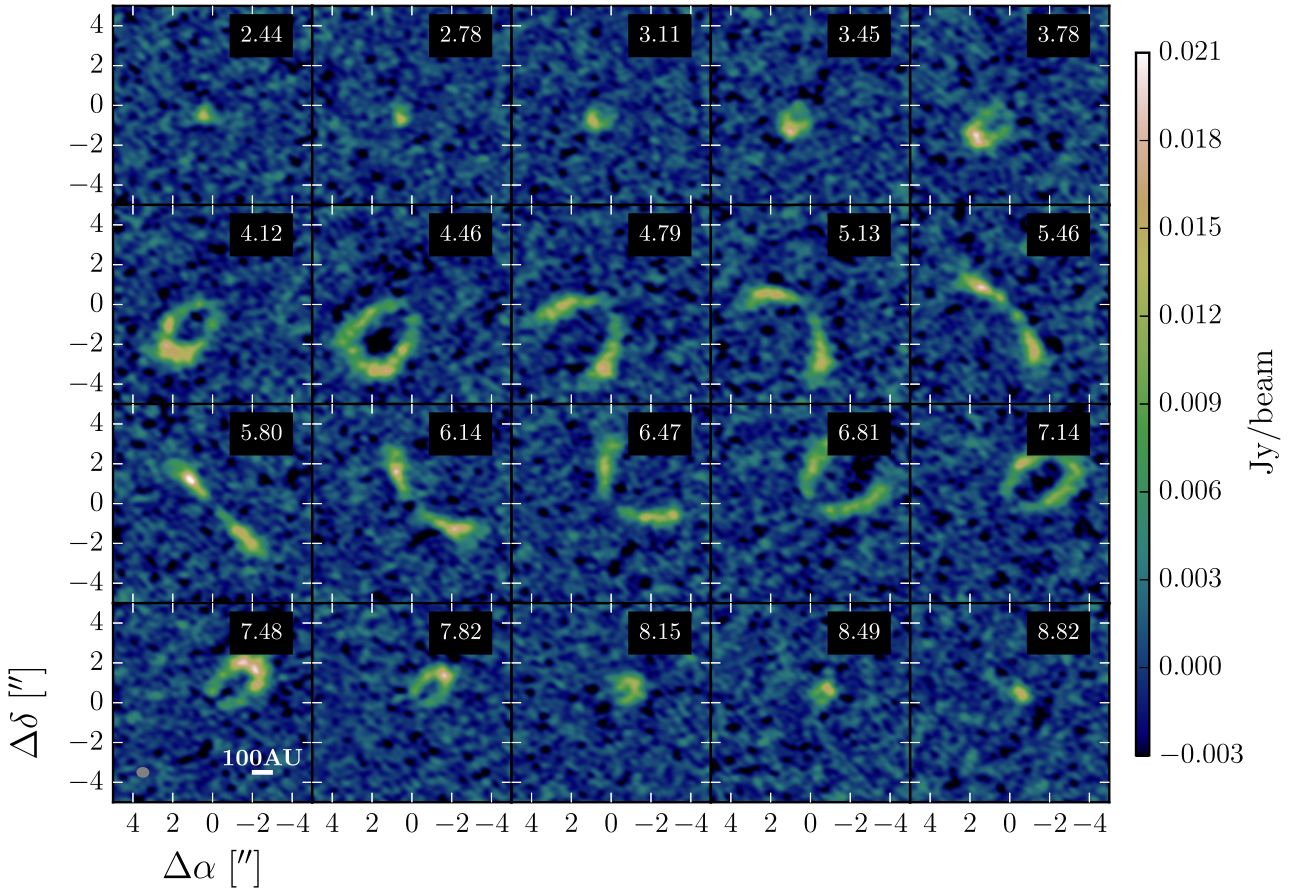


Fig. 3: Channel maps of $\text{H}_2\text{CO } 3_{03}-2_{02}$ from $2.44-8.82 \text{ km s}^{-1}$, Hanning smoothed to 0.336 km s^{-1} channels. Channel velocity is shown in the upper-right corner. Synthesized beam and AU scale are shown in the lower-left panel.

citation temperature. Physical parameters of the three lines and the continuum can be found in Table 1.

HD 163296 has a V_{LSR} systemic velocity of $+5.8 \text{ km s}^{-1}$ (Qi et al. 2011), which corresponds well to the central velocity of the $\text{H}_2\text{CO } 3_{03}-2_{02}$ line. The $\text{H}_2\text{CO } 3_{03}-2_{02}$ line flux was derived after masking pixels with $< 3\sigma$ emission in the image cube. The cube was then integrated spatially over a $7''$ radius and over velocity channels $0.76 - 10.84 \text{ km s}^{-1}$. Lower limits

on $\text{H}_2\text{CO } 3_{22}-2_{21}$ and $\text{H}_2\text{CO } 3_{21}-2_{20}$ line fluxes are from estimates via the matched-filter method. Upper limits on the lines are based on spectra from the CLEAN images of $\text{H}_2\text{CO } 3_{22}-2_{21}$ and $\text{H}_2\text{CO } 3_{21}-2_{20}$ and are given at the $3\sigma_1$ level, where $\sigma_1 = 0.5 \sqrt{\pi/\log(2)} \Delta\nu \sigma_{\text{rms}}$ estimates the area of a Gaussian curve, $\Delta\nu$ is the FWHM of the detected $\text{H}_2\text{CO } 3_{03}-2_{02}$, and σ_{rms} is the rms noise in Jy from the disk-integrated spectra.

The H₂CO 3₀₃–2₀₂ image has a 0.54'' × 0.42'' [66 × 51 AU] synthesized beam (P.A. = 86.5°). Figure 2 shows a velocity-weighted (first-order moment) map of H₂CO 3₀₃–2₀₂ from 0.76 – 10.84 km s⁻¹, clipped at the 3σ level, which reveals the full extent of the H₂CO emission in Keplerian rotation, while Figure 3 shows the channel maps of H₂CO 3₀₃–2₀₂ around HD 163296 Hanning smoothed to a resolution of 0.336 km s⁻¹ over velocities where molecular emission is present. The inner and outer projected radii ($i = 44.0^\circ$, P.A. = 133° East of North) of H₂CO 3₀₃–2₀₂ emission at the 3σ level along the major axis are 0.4'' and 4.5'', respectively, corresponding to projected physical distances $R_{\text{in}} \approx 50$ AU and $R_{\text{out}} \approx 550$ AU at a distance of 122 pc (van den Ancker et al. 1998).

The extent of H₂CO 3₀₃–2₀₂ was found to be greater than that of the 1.3 mm continuum (shown in black contours in Figure 2), suggesting that millimeter-sized grains have decoupled from the gas and drifted radially inward. de Gregorio-Monsalvo et al. (2013) observed the same phenomenon in ¹²CO and the 850 μm continuum. The 1.3 mm continuum has a projected outer radius at 3σ of 2.2'', or $R_{\text{out}}^{1.3\text{mm}} \approx 270$ AU. The 1.3 mm emission extends beyond the 850 μm continuum reported by de Gregorio-Monsalvo et al. (2013) due to the increased sensitivity of our observations. Zhang et al. (2016) reported that analysis of the 1.3 millimeter continuum visibilities in this data set suggests a ring-like structure not seen in imaging at this resolution. The ring-like nature of the millimeter dust was confirmed by high-resolution observations after the original submission of our paper (Isella et al. 2016). They explained the dust morphology as three distinct dust gaps centered at 60, 100, and 160 AU.

To calculate the H₂CO 3₀₃–2₀₂ radial intensity profile, an integrated intensity (zero-order moment) map was first created by applying a mask in right ascension, declination, and velocity to the image cube to enhance the signal-to-noise. The mask is based on the disk rotational velocity profile, which is assumed to be Keplerian with a mass of $M = 2.3 M_\odot$, corresponding to the mass of the central star. In each velocity channel of the image cube, a subset of pixels were chosen where the calculated Keplerian velocity of the pixels matches the Doppler-shifted velocity of the line. All pixels that did not match these criteria were masked. Yen et al. (2016) use a similar method to extract their integrated intensity maps. The radial intensity profile and integrated intensity map for H₂CO 3₀₃–2₀₂ emission are shown in Figure 2. Azimuthally-averaged elliptical annuli projected to an inclination of 44° and position angle of 133° were used to calculate the average flux in each radial step. This method provides more signal-to-noise per annulus, but results in a decrease in resolution by a factor of two due to the foreshortening along the inclined disk's minor axis in our radial intensity profiles. Radial step sizes of 0.24'' for H₂CO 3₀₃–2₀₂ and 0.4'' for C¹⁸O 2–1 were used for each annulus to provide a sampling of approximately two data points per original beam width.

The radial profile reveals an absence of emission at the center of the disk, a peak in intensity at ~100 AU with emission then decreasing until a turnover in the profile at ~200 AU and a bump at ~300 AU, signifying an enhancement in emission in the outer regions of the disk. The same curve for C¹⁸O has centrally peaked emission and intensity decreasing with radius. Already the shape of the radial profiles of the two molecules indicates a difference in abundance gradients throughout the disk. The C¹⁸O profile suggests that it follows more or less the smoothly decreasing H₂ gas density. On the other hand, H₂CO shows a peak at the approximate location of the CO snow line at 90 AU (Qi et al. 2015), and another enhancement is located roughly at the edge of the dust continuum. Such a radial profile highlights the

need for two H₂CO formation mechanisms to account for the observed emission: one warm route that produces emission at temperatures above that of CO freeze-out in the inner disk within 100 AU and one cold route that produces emission outside of the CO snow line. Further explanations for these features are given in Section 3.2 and Section 4.

3.1.1. Matched filter detections

After subtracting the continuum from the line data, we employed a matched filter technique to the visibilities to detect the weaker H₂CO 3₂₂–2₂₁ and H₂CO 3₂₁–2₂₀ lines. In this technique, an image cube containing a template emission profile is sampled in uv space to obtain a set of template visibilities that act as the filter. The template is then cross-correlated with a set of visibilities with a low signal-to-noise ratio (SNR) in an attempt to detect the presence of the template emission within the low SNR data set. The cross-correlation is done by sliding the template visibilities channel-by-channel across the velocity axis of the low SNR visibilities. When the template reaches the source velocity in the low SNR data, there will be a sharp peak in the filter response spectrum of the correlation if the template signal is detected within the low SNR visibilities. This is analogous to image-based stacking approaches (e.g. Yen et al. 2016), but retains the advantages of working in the uv plane. In this work, to obtain a data-based template for the matched filter method, the H₂CO 3₀₃–2₀₂ line was re-imaged with CLEAN in 0.084 km s⁻¹ velocity channels using a uv taper to achieve a 1'' synthesized beam. Image channels showing H₂CO emission (1.6–10 km s⁻¹) were sampled in the uv plane using the PYTHON `vis_sample`² routine, and the resulting visibilities were then used as the template signal.

Figure 4 shows the filter impulse responses of the three H₂CO visibility data sets to the H₂CO 3₀₃–2₀₂ template. The black curve is the response of the H₂CO 3₀₃–2₀₂ visibility data to the template, highlighting the effectiveness of the filter to recover the line detection. The inset reveals the 4.5σ and 5σ detections of H₂CO 3₂₂–2₂₁ and H₂CO 3₂₁–2₂₀, respectively, where σ is

² `vis_sample` is publicly available at https://github.com/AstroChem/vis_sample or in the Anaconda Cloud at https://anaconda.org/rloomis/vis_sample

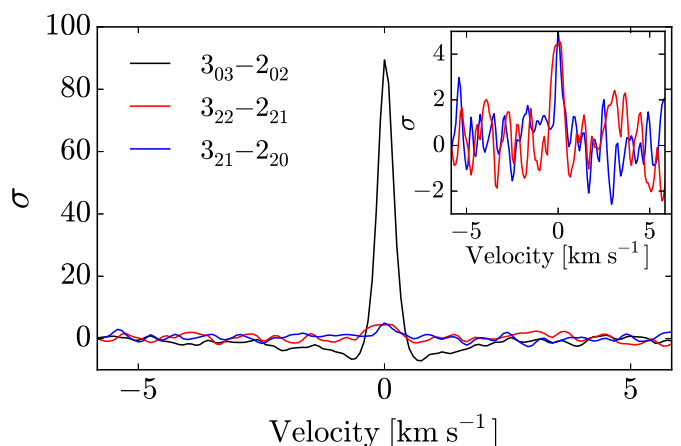


Fig. 4: Matched filter responses of the observed H₂CO lines to the H₂CO 3₀₃–2₀₂ data-based template. Self-response (black) shows template recovery of the 3₀₃–2₀₂ detection. *Inset:* H₂CO 3₂₂–2₂₁ (red) and H₂CO 3₂₁–2₂₀ (blue) are detected at the 4.5σ and 5σ level, respectively.

calculated as the standard deviation of the response of emission-free visibility channels to the template. To constrain the total flux of the weaker lines, we compare the ratio of their peak filter responses and the peak response of the $\text{H}_2\text{CO } 3_{03-2_{02}}$ visibilities (90σ , Figure 4). Under the assumption that all three observed H_2CO lines are co-spatial, the σ -ratio can be used to estimate the weaker line fluxes reported in Table 1. The response of the template is limited by how well it spatially matches the emission, thus making the derived line fluxes lower limits.

3.2. Modeling H_2CO and C^{18}O emission

Previous studies (Qi et al. 2011; Rosenfeld et al. 2013; Qi et al. 2015) have attempted to use CO isotopologues to determine the radial location of CO freeze-out in HD 163296. Qi et al. (2011) modeled the ^{13}CO isotope and found a distinct drop in abundance at ~ 155 AU, which they attributed to CO freeze-out. However, in Qi et al. (2015) they claim ^{13}CO is a less robust tracer as it is difficult to separate CO freeze-out from opacity effects. ^{13}CO may remain optically thick out to radii beyond 100 AU. Thus, the apparent depletion may be due to a decrease in optical depth rather than an actual drop in abundance. They use C^{18}O as a more robust, optically thin tracer of the column density of CO throughout the disk. Following this reasoning, we model only the C^{18}O isotopologue to reveal structure in the CO gas. Although the C^{18}O Science Verification data has been previously reported (Rosenfeld et al. 2013; Qi et al. 2015), we reanalyze the data in an effort to provide a ground truth for the CO surface density – particularly for the outer disk – within the same modeling approach as used for H_2CO and within the limits of the data resolution and our disk model.

The aims of modeling H_2CO and C^{18}O are to determine likely formation scenarios for H_2CO and any relation to the CO snow line. If H_2CO is abundant in regions close to or below the CO freeze-out temperature, grain surface formation of H_2CO on CO ices will contribute. If H_2CO is abundant only at high temperatures zones of the disk, then gas-phase production of H_2CO dominates. By varying the relative molecular abundances in different regions of the models and comparing the model distribution to the data, we can determine which parts of the disk are harboring reservoirs of H_2CO .

This section describes the models used to reproduce the observed $\text{H}_2\text{CO } 3_{03-2_{02}}$ and $\text{C}^{18}\text{O } 2-1$ emission based on the HD 163296 disk model created by Qi et al. (2011). In their paper they constrain the radial and vertical density and temperature structure of a steady viscous accretion disk with an exponentially-tapered edge. Fitting the model continuum at multiple wavelengths to the observed SED constrained the radial structure. Observations of multiple optically thick ^{12}CO transitions were used to constrain the vertical structure. A modified version of this physical model was used by Mathews et al. (2013) to determine the distribution of DCO^+ in HD 163296. To constrain the vertical structure of the dust in our physical model, Mathews et al. (2013) refit the SED by varying independently the dust scale heights of Gaussian distributions of small ($a_{\text{max}} = 25 \mu\text{m}$) and large ($a_{\text{max}} = 1 \text{mm}$) populations of dust grains. Similarly, the vertical gas density distribution is treated as a two-component model with independent scale heights to simulate a Gaussian distribution at low heights with an extended tail higher in the disk. The gas scale heights are varied to recover the CO fluxes reported in Qi et al. (2011). Given these dust and gas distributions and assuming the dust continuum to be optically thin, the gas surface density of both H_2CO and C^{18}O should be robustly measured in our models.

In this work, the Mathews et al. (2013) model was used as the physical disk structure for simulating molecular emission using the LIME Modeling Engine (LIME, Brinch & Hogerheide 2010) 3D radiative transfer code. Synthesized data cubes were created with LIME for $\text{H}_2\text{CO } 3_{03-2_{02}}$ and $\text{C}^{18}\text{O } 2-1$ in non-LTE with H_2 as the primary collision partner. Both ortho- and para- H_2 species were included in collisional excitation, with a temperature-dependent ortho- to para- ratio (OPR) such that $\text{OPR} = 3$ at temperatures ≥ 200 K and decreases exponentially at lower temperatures. Molecular collision rates were taken from the Leiden Atomic and Molecular Database (LAMDA, Schoeier et al. 2005). The disk inclination, position angle, and distance are set to $i = 44.0^\circ$, P.A. = 133.0° , and $d = 122 \text{pc}$.

Four types of models are used to test the distribution of observed $\text{H}_2\text{CO } 3_{03-2_{02}}$ with different fractional abundance profiles relative to H_2 . Figure 5 depicts examples of each of these scenarios with the relevant disk regions. Three of these models are used for $\text{C}^{18}\text{O } 2-1$. The first model assumes a constant abundance constrained to low temperatures where H_2CO formation on the surface of icy grains is favorable (Section 3.2.1). The low-temperature model is not used for $\text{C}^{18}\text{O } 2-1$. In the second model, $\text{H}_2\text{CO } 3_{03-2_{02}}$ and $\text{C}^{18}\text{O } 2-1$ have a power-law abundance profile (Section 3.2.2). The third model has a temperature-based step-abundance profile with a constant inner (high-temp) and outer (low-temp) abundance and a change-over temperature T_c as the boundary (Section 3.2.3). The final model has a radial step-abundance profile with a constant inner abundance, constant outer abundance, and change-over radius R_c (Section 3.2.4). Analysis of the models makes use of the `vis_sample` routine to read the uv coordinates directly from an observed ALMA measurement set and create synthetic visibilities based on an input sky model.

A central hole is observed in the H_2CO data, as seen in Figure 2, with a size approximately equal to the width of the beam. This hole is likely a result of strong absorption by an optically thick dust continuum (see also Section 4.2). Beyond 50 AU, the optical depth radial profile for the LIME model continuum is found to be optically thin with $\tau < 0.6$, which ensures that features in the gas radial profile outside of 50 AU are not caused by dust opacity effects. The inner region (< 50 AU) cannot be properly modeled here due to the low resolution of the observations, which do not allow for proper description of any dust substructure. The modeling of Zhang et al. (2016) and new high-resolution observations by Isella et al. (2016) show significant substructure in the dust and a large increase in optical depth in the inner 50 AU. Such substructure is unlikely to be accurately described in our models, thus we ignore radii < 50 AU. The central hole is therefore treated as an H_2CO abundance inner radius in the modeling.

All $\text{H}_2\text{CO } 3_{03-2_{02}}$ models have an inner radius set to $R_{\text{in}} = 50$ AU. R_{in} was constrained for H_2CO by varying the inner radius of a constant abundance model to determine the best fit to the inner 150 AU of the radial intensity curve. Thereafter, R_{in} remains a fixed parameter in the models. $\text{C}^{18}\text{O } 2-1$ models have no such inner radius as the emission is centrally peaked.

Each LIME model was continuum-subtracted before running `vis_sample`. We first tested $\text{H}_2\text{CO } 3_{03-2_{02}}$ and $\text{C}^{18}\text{O } 2-1$ models normalized to the total flux of the data in order to find the best-fit to the spatial distribution of each line, then we varied the abundance of the best-fit normalized model to match the absolute flux of the data. To determine the total flux, we took a vector average of visibilities with baselines $< 30 \text{m}$ and integrated over all channels containing emission. The model was then scaled to match the total flux of the data. Goodness of fit for each model

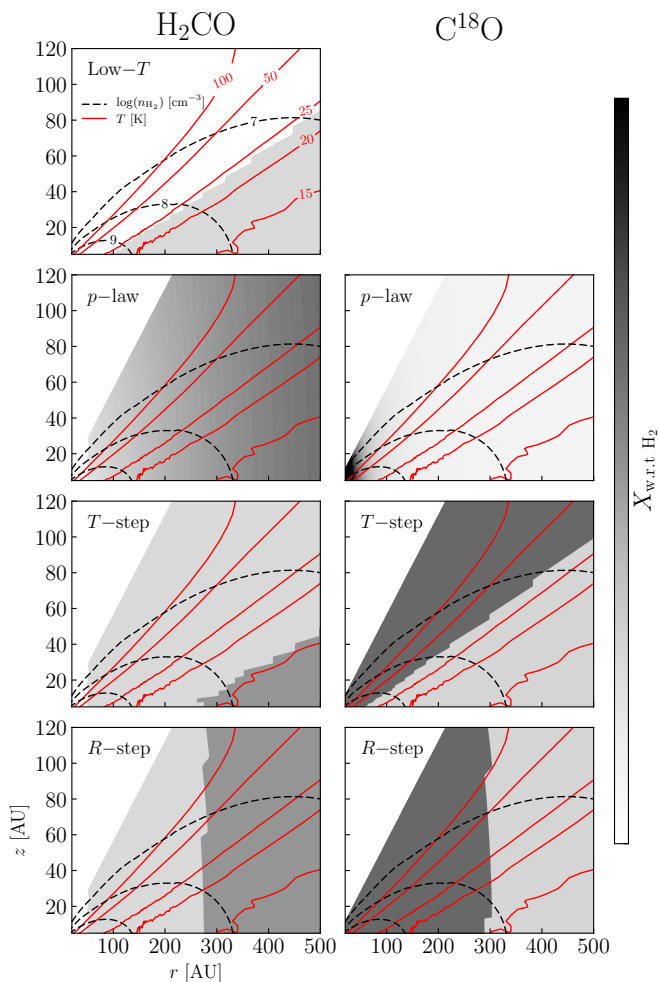


Fig. 5: Toy model abundance scenarios for H₂CO (left) and C¹⁸O (right). X is the molecular abundance with respect to molecular hydrogen (grayscale). Red solid contours show the temperature structure of the gas in the disk. Black dashed contours show the density structure of the gas in the disk as the log of the molecular hydrogen number density. The X distribution in each panel follows the best-fit normalized model (Table 2).

was determined by χ^2 minimization between the normalized visibilities of the model and the visibilities of the data. Initial reference abundances were chosen for the normalized models to ensure optically thin line emission. The H₂CO reference abundance was set to $X = 1.0 \times 10^{-12}$. C¹⁸O models used a reference abundance of $X = 1.0 \times 10^{-7}$. All normalized models remained optically thin with $\tau < 1$; there was no significant increase in the optical depth profile of the models for the parameter space explored here. The best-fit normalized model for each line was then used to vary the molecular abundances to find the best agreement between the absolute flux of the model and of the data using χ^2 minimization on the visibilities.

3.2.1. Low-temperature abundance model

The low-temperature model simulated H₂CO emission that is present due to grain-surface chemistry in regions below the expected CO freeze-out temperature and subsequent non-thermal desorption from icy grains. The models used a constant fractional abundance relative to H₂, constrained by a threshold tem-

Table 2: Best-Fit Normalized Models

H ₂ CO 3 ₀₃ –2 ₀₂					
Abundance Model	p	T_c [K]	R_{in}^a [AU]	R_c [AU]	X_1/X_2
Low-temperature	–	24±2	–	65±15 [†]	–
Power-law	+0.5	–	50	–	–
Temperature step	–	16±2	50	230±60 [†]	0.5
Radial step	–	15±1 [†]	50	270±20	0.5
C ¹⁸ O 2–1					
Abundance Model	p	T_c [K]	R_{in}^a [AU]	R_c [AU]	X_1/X_2
Power-law	–2	–	0.1	–	–
Temperature step	–	32±2	0.1	32±5 [†]	10
Radial step	–	15±1 [†]	0.1	290±20	10

Notes. χ^2 values are reduced by the number of points and free parameters in each model. ^(a) Fixed parameter. ^(†) Indicates the corresponding midplane value to the best-fit model parameter based on the density and temperature structure of the Mathews et al. (2013) physical model.

perature. Above the threshold temperature the H₂CO abundance was set to zero everywhere. Based on estimates of CO freeze-out temperatures from Qi et al. (2015), model threshold temperatures range from 14–50 K in steps of 2 K. Below the threshold temperature, gas-phase H₂CO is present. It is assumed that there is a mechanism to stimulate sufficient desorption of H₂CO from the icy grains, such as UV or X-ray photodesorption, or cosmic rays penetrating the disk midplane.

The best fit for the normalized low-temperature model for H₂CO has a threshold temperature of 24±2 K, corresponding to a midplane radius of 65±15 AU. Seen in Figure 6, the model radial intensity curve fails to recover the sharp decrease in emission between 100–200 AU and the turnover and secondary bump beyond ~200 AU. It is clear that a scenario in which H₂CO originates entirely beyond the CO freeze-out temperature is not a good representation of the distribution seen in the observations. There must be H₂CO present in other parts of the disk.

3.2.2. Power-law abundance model

In these models a varying abundance profile was considered for both H₂CO and C¹⁸O, following a power-law distribution,

$$X = X_{100\text{AU}} \left(\frac{R}{100 \text{ AU}} \right)^p,$$

where $X_{100\text{AU}}$ is the abundance at 100 AU, R is the disk radius, and p is the power-law index. C¹⁸O is present throughout the disk. H₂CO has an inner radius $R_{in} = 50$ AU, which was used in all subsequent H₂CO modeling.

The best-fit power-law H₂CO model has $p = 0.5$, with the abundance increasing with radii. The best-fit value found here is more gradual than the $p = 2$ positive power law slope found by Qi et al. (2013), but both suggest that there is increased H₂CO production occurring in the outer disk. However, the $p = 0.5$ model does not provide the overall normalized best fit to the H₂CO 3₀₃–2₀₂ data presented here, as seen in Figure 6. The best-fit C¹⁸O model had $p = -2$, suggesting C¹⁸O is centrally peaked, but with a decreasing abundance in the outer regions of the disk. The model radial intensity curve under-produces emission beyond 200 AU and overproduces emission inside of 200 AU.

The simple power-law model does not capture the distribution seen in either H₂CO or C¹⁸O. The failure of the H₂CO model to recover the shape of the radial intensity profile suggests that there are changes in the distribution of emission not

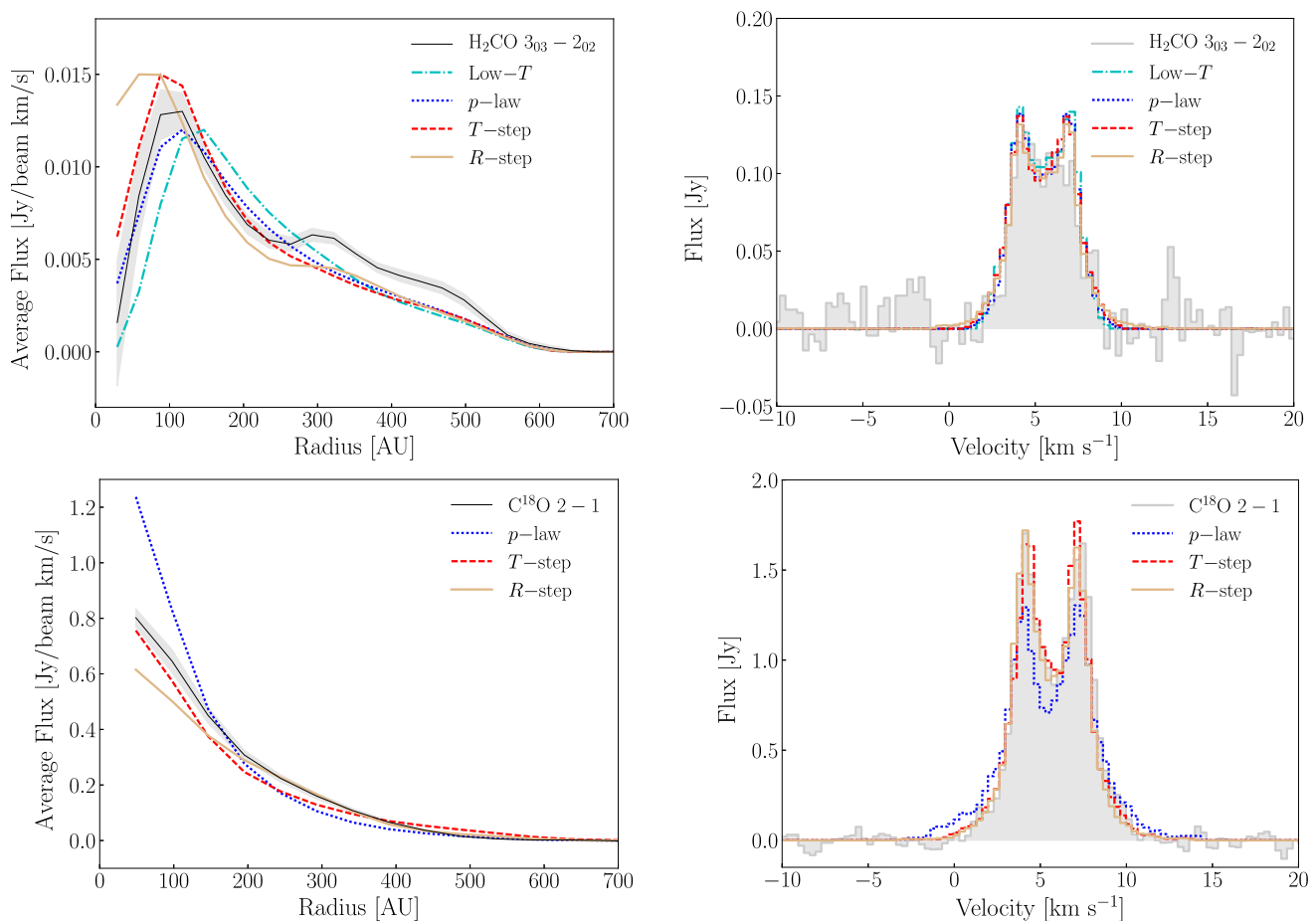


Fig. 6: $\text{H}_2\text{CO } 3_{03}-2_{02}$ and $\text{C}^{18}\text{O } 2-1$ data are compared with best-fit normalized models for each scenario mentioned in Section 3.2. The low-temperature model (dot-dashed cyan), the power-law model (dotted blue), the temperature step-abundance model (dashed red), and the radial step abundance model (solid gold) show the radial distribution and spectra. (Left) Radial intensity curves of the best-fit normalized models obtained from azimuthally-averaged elliptical annuli projected to $i=44^\circ$, P.A.= 133° . The shaded grey region represents 1σ error bars. H_2CO profiles are taken from integrated intensity maps after applying a Keplerian mask. (Right) Disk-integrated spectra of the best-fit normalized models obtained from a $5.6''$ circular aperture. H_2CO spectra are Hanning smoothed to 0.336 km^{-1} channels. Parameters for each model can be found in Table 2.

captured in this model; we are underestimating the contribution from grain surface formation. The failure of the C^{18}O power-law model indicates that the effect of CO depletion is not properly taken into account. To reproduce the data at our resolution, the C^{18}O abundance profile needs an abrupt change rather than the gradual change provided by the power-law model.

3.2.3. Temperature step-abundance model

Two-phase abundance models with a change-over temperature that distinguishes between the warm and cold regions of the disk were created to test H_2CO formed in the gas phase and H_2CO originating from icy grains, respectively. We assume that the change-over temperature represents the boundary below which H_2CO should form via hydrogenation of CO ice. The temperature step-abundance model for C^{18}O reflects the freeze out of CO, both radially and vertically, since there also is a vertical temperature gradient. While in these models we parameterize the C^{18}O abundance with a change-over temperature, it is important to remember that this results in a radial column density profile that decreases gradually and extends well beyond the midplane CO snow line. Given our limited angular resolution, our data pri-

marily samples the radial extent of the disk surface layer where C^{18}O is present in the gas phase. Although we parameterize this with a temperature, we caution against the simplistic interpretation as an evaporation temperature, since its value depends on how well we know the vertical temperature structure and because our data do not resolve the location of the midplane CO snow line.

The change-over temperature T_c was tested in the range 12 – 36 K in steps of 2 K. The abundance ratio between the inner and outer regions varies to cover the range X_1/X_2 from 0.001 – 10 (0.1 – 1000 for C^{18}O). The best-fit H_2CO model has a change-over temperature $T_c = 16 \pm 2 \text{ K}$ and an abundance ratio $X_1/X_2 = 0.5$, indicating a factor of 2 enhancement of H_2CO in the outer regions, but the model does not reproduce emission beyond 200 AU well (Figure 6). C^{18}O is best fit by a change-over temperature $T_c = 32 \pm 2 \text{ K}$ with an order of magnitude reduction ($X_1/X_2 = 10$) in the outer regions. The temperature step-abundance model provides an improved normalized fit to the C^{18}O observational data over models 1 & 2 and is consistent with CO depletion in the cold, outer disk.

As explained above, we do not claim that T_c is the evaporation temperature of CO, but rather that the value of T_c results

in a reasonable match of the radial column density distribution of C¹⁸O given our adopted temperature structure and the limited angular resolution of the data. Even then, the radial profile of this model under-produces C¹⁸O within ~400 AU and overproduces C¹⁸O outside of ~400 AU.

While this model provides a better fit to the H₂CO emission than models 1 & 2, it fails to recover the shape of the turnover in the radial profile seen at ~200 AU. Instead, the temperature-based boundary causes a gradual change in the radial intensity due to the vertical temperature structure in the disk. To better fit the turnover seen in the radial profile, the H₂CO abundance profile must have an even more abrupt radial change. The improvement of the C¹⁸O normalized model fit over models 1 & 2 suggests CO freeze-out in the cold, outer parts of the disk.

3.2.4. Radial step-abundance model

In these models, molecular gas abundance is constant throughout the vertical extent of the disk with different abundance values in the inner and outer regions across the change-over radius. The outer abundance was varied such that X_1/X_2 spanned 0.1 – 10 for H₂CO and 0.1 – 1000 for C¹⁸O. The change-over radius R_c ranged from 210 – 410 AU for H₂CO and 70 – 350 for C¹⁸O in steps of 20 AU.

The radial step-abundance model reproduces the turnover seen in the radial intensity of the H₂CO emission better than the first three models. Best-fit parameters are a change-over radius $R_c = 270 \pm 20$ AU and an abundance ratio $X_1/X_2 = 0.5$. The radial step-abundance model gives a radial intensity profile that has a steep drop between ~100–200 AU and a sharp turnover and plateau beyond ~200 AU. Best-fit C¹⁸O models have $R_c = 290 \pm 20$ AU and $X_1/X_2 = 10$, indicating a factor of ten depletion of CO in the outer disk beyond the edge of the millimeter grains. This abundance scenario also provides a better normalized fit than models 1 & 2, and reproduces the distribution of C¹⁸O as well as model 3.

In this model the H₂CO bump in the radial intensity curve is well-captured due to the sharp change in abundance across the change-over radius. The radial step-abundance model provides the right amount of H₂CO production in the inner and outer regions, likely a combination of gas-phase and grain-surface formation. Penetrating UV photons could photodesorb H₂CO that has formed via hydrogenation of CO ices beyond ~300 AU. There may also be more gas-phase H₂CO formation beyond the edge of the millimeter continuum at ~270±20 AU if UV photons can photodissociate CO in the upper layers and activate hydrocarbon chemistry for a more efficient CH₃ + O pathway. The C¹⁸O radial step-abundance model provides an alternative scenario for outer disk CO depletion compared to model 3. If the micron-sized grains are depleted in the outer disk similar to the millimeter-sized grains, UV photons could photodissociate CO beyond ~300 AU.

The fact that both a radial step at 290±20 AU and a temperature step at 32±2 K (32±5 AU near the midplane) equally well fit the C¹⁸O data underlines our caution against interpreting the value of T_c as the evaporation temperature. The consequences of each model scenario are further discussed in Section 4. The radial step-abundance case is chosen as the C¹⁸O normalized model for estimating abundances in Section 3.2.5.

3.2.5. H₂CO and C¹⁸O abundance

To estimate the absolute fractional abundances relative to H₂ in the inner and outer regions for H₂CO and C¹⁸O, LIME was used to vary the abundances for the best-fit normalized scenarios. Abundance ratios across the change-over boundaries, R_c , were kept the same as the normalized models: $X_1/X_2 = 0.5$ for the H₂CO radial step-abundance model and $X_1/X_2 = 10$ for the C¹⁸O radial step-abundance model.

H₂CO models had $R_c = 270$ AU and $X_1 = [1.0, 2.0, 3.0, 4.0, 5.0] \times 10^{-12}$. The best-fit fractional abundances were $X_1 = 4.0 \times 10^{-12}$ and $X_2 = 8.0 \times 10^{-12}$. C¹⁸O was found to have best-fit fractional abundances of $X_1 = 5.0 \times 10^{-8}$ and $X_2 = 5.0 \times 10^{-9}$ with $R_c = 290$ AU. Radial intensity profiles for these best-fit models are shown in Figure 7. Error estimates based 3 σ error bars of the radial intensity profiles put these abundances in the range $X_1 = 2-5 \times 10^{-12}$, $X_2 = 5-10 \times 10^{-12}$ for H₂CO and $X_1 = 4-12 \times 10^{-8}$ and $X_2 = 4-12 \times 10^{-9}$ for C¹⁸O.

Integrated intensity maps of the best-fit models were compared to integrated intensity maps of observed H₂CO 3₀₃–2₀₂ and C¹⁸O 2–1 data. Figure 8 shows the images and the residuals. The model and the data are in good agreement for both lines, though the best-fit C¹⁸O has residual emission above the 3 σ in the central part of the disk. The inner 50 AU are likely not well-described by our models, as noted in Section 3.2.

The modeling efforts presented here show that the H₂CO abundance is not uniform throughout the disk. Beyond ~300 AU there is an increase in the H₂CO abundance by a factor of two, as seen in the radial step-abundance scenario. The H₂CO abundance of $X_1 = 2-5 \times 10^{-12}$, $X_2 = 4-10 \times 10^{-12}$ is consistent to within a factor of a few with the global abundance value of 1×10^{-11} found in Qi et al. (2013). The increased sensitivity and resolution of our data allow us to better constrain the H₂CO abundance in HD 163296 than previous studies. C¹⁸O is well-described by a model with a depletion of CO at 290±20 AU and a depletion factor of ten. The C¹⁸O inner abundance of 4–12×10⁻⁸ corresponds to a ¹²CO abundance of 2.2–6.6 × 10⁻⁵, assuming ¹²CO/C¹⁸O = 550. Qi et al. (2015) report similar numbers for the CO abundance, but their depletion factor is lower by half and occurs at a radius of 90 AU. We found that a radius of 90 AU and depletion factor of 5 for our radial step-abundance models significantly overproduces the amount of C¹⁸O beyond 300 AU due to our different treatment of the vertical structure.

3.3. H₂CO excitation temperature

Line flux ratios H₂CO 3₀₃–2₀₂/H₂CO 3₂₂–2₂₁ and H₂CO 3₀₃–2₀₂/H₂CO 3₂₁–2₂₀ were used to constrain H₂CO excitation temperatures. Table 1 provides the line fluxes. We calculated the rotational temperature of the lines, assuming a single rotational temperature, following Qi et al. (2013)

$$T_{\text{rot}} = \frac{E_1 - E_0}{\ln((\nu_1 S \mu_1^2 \int T_0 dv) / (\nu_0 S \mu_0^2 \int T_1 dv))}, \quad (1)$$

with the following definitions: E_0 and E_1 are the upper energy levels for the low and high H₂CO transitions, respectively; ν is the line frequency; $S \mu^2$ is the temperature-independent transition strength and dipole moment; and $\int T dv$ is the integrated line intensity. Line intensity in the Rayleigh-Jeans limit was calculated from the line flux with the following expression

$$T_{\text{B}} = \frac{c^2}{2k\nu^2} \frac{F_{\nu}}{(a \times b)} \left(3600 \frac{\text{arcsec}}{\text{deg}} \right)^2 \left(\frac{180 \text{ deg}}{\pi \text{ sr}} \right)^2 \left(\frac{1}{10^{26} \text{ Jy}} \right), \quad (2)$$

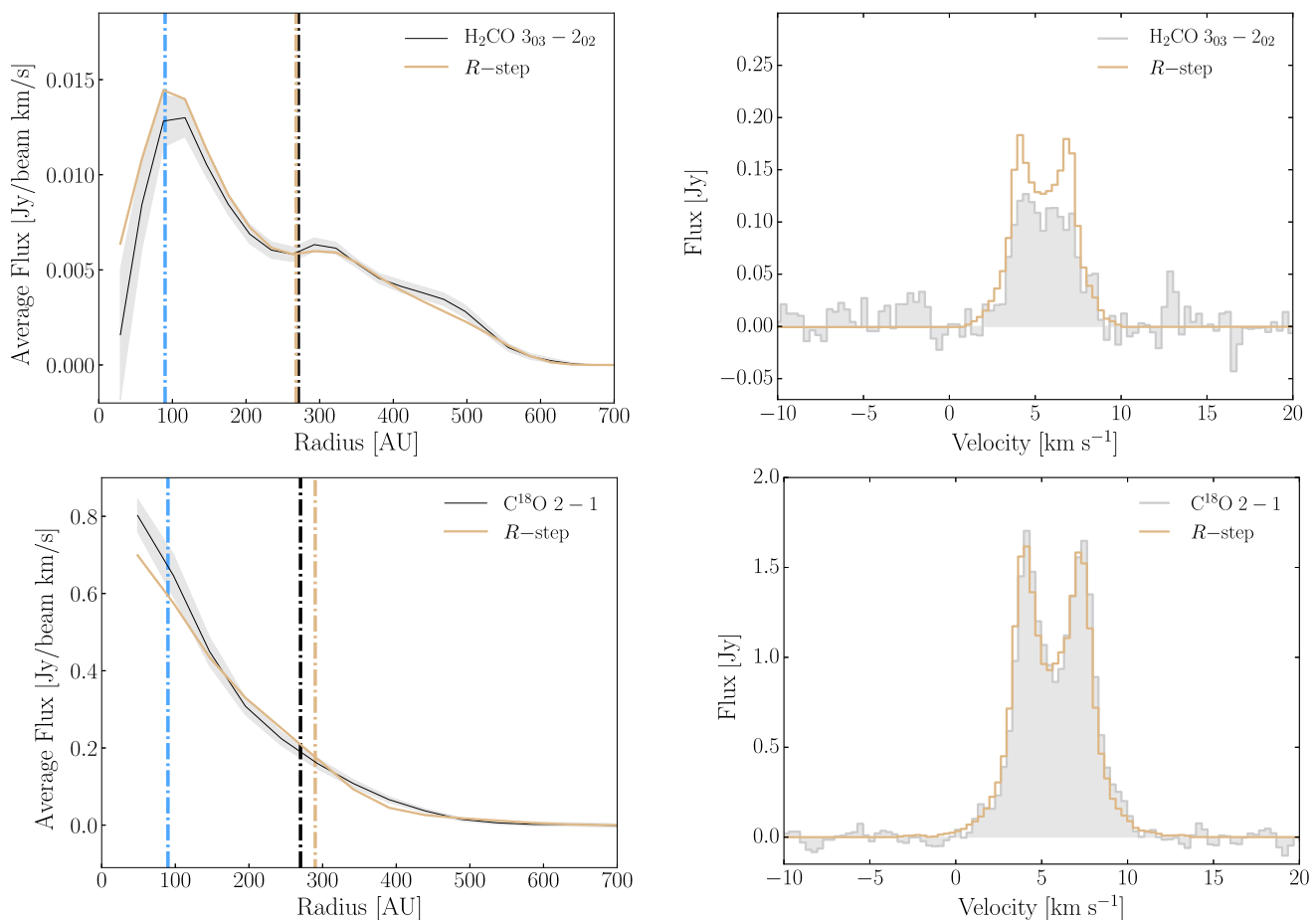


Fig. 7: Radial intensity and spectra of observed $\text{H}_2\text{CO } 3_{03}-2_{02}$ and $\text{C}^{18}\text{O } 2-1$ versus the best-fit models. (*Left*) Radial intensity curves from azimuthally-averaged elliptical annuli projected to $i=44^\circ$, P.A.= 133° . HD 163296 data is shown in black, best-fits for H_2CO and C^{18}O are in gold. The vertical dashed lines indicate the CO snow line (blue dash) from Qi et al. (2015), the 5σ outer radius of the 1.3 mm grains (black dash), and the change-over radii, R_c , for the best-fit radial step-abundance models (gold dash). H_2CO profiles are taken from integrated intensity maps after applying a Keplerian mask. (*Right*) Disk-integrated spectra. HD 163296 data is shown in filled gray. H_2CO spectra are Hanning smoothed to 0.336 km^{-1} channels.

where F_ν is the line flux in Jy, T_B is the line intensity in Kelvins, ν is the line frequency in Hz, k is the Boltzmann constant, c is the speed of light, and a and b are the semi-major and semi-minor axes of the beam in arcsec.

The emitting regions of all three lines are expected to be similar, especially if the H_2CO reservoir is primarily locked up in icy grains. LTE is a fair assumption for calculating rotational temperatures, as the gas density near the midplane is high in disks ($\sim 10^9 \text{ cm}^{-3}$; Walsh et al. 2014) and the critical densities of the observed transitions at 20 K are $1-3 \times 10^6$ (Wiesenfeld & Faure 2013). In the case of LTE, the derived rotational temperature is equal to the kinetic temperature of the gas. E and $S\mu^2$ are taken from the CDMS (Müller et al. 2005), as reported on the Splatalogue³ database.

The rotational temperatures of the H_2CO transitions are calculated based on the line flux ratios of $\text{H}_2\text{CO } 3_{22}-2_{21}/3_{03}-2_{02}$ and $\text{H}_2\text{CO } 3_{21}-2_{20}/3_{03}-2_{02}$. The matched-filter technique only gives lower limits to the $\text{H}_2\text{CO } 3_{22}-2_{21}$ and $\text{H}_2\text{CO } 3_{21}-2_{20}$ line flux, thus lower limits on the rotational temperature are $>20.5 \text{ K}$ and $>19.5 \text{ K}$, respectively, while upper limits for the weak lines are $<169 \text{ K}$ and $<326 \text{ K}$ based on the integrated flux upper limits listed in Table 1. These lower limits indicate that these transi-

tions can be excited in regions of the disk near the CO freeze-out temperature, supporting the hypothesis that some of the H_2CO emission may originate from the cold molecular reservoir. There could also be H_2CO emitting at a higher temperature that is not well described by our template filter.

4. Discussion

In this work, the radial step-abundance model suggests an enhancement in H_2CO abundance by a factor of a few beyond 270 AU. It is difficult to distinguish which formation route is responsible for this modest increase in abundance.

Aikawa & Herbst (1999) estimated the radial column density and abundance profile of H_2CO formed in the gas phase in a T Tauri minimum mass solar nebula (MMSN) disk model extrapolated out to $R_{out} = 700 \text{ AU}$, with an order of magnitude lower mass. They did not consider other mechanisms for producing gas-phase H_2CO , such as desorption from icy grains. They exclude an activation energy barrier for the $\text{CH}_3 + \text{O}$ reaction. The initial abundance of atomic oxygen may affect the inferred H_2CO abundances. Their model has a mostly flat radial distribution, but is consistent with an enhancement of H_2CO abundance

³ <http://www.cv.nrao.edu/php/splatalogue/>

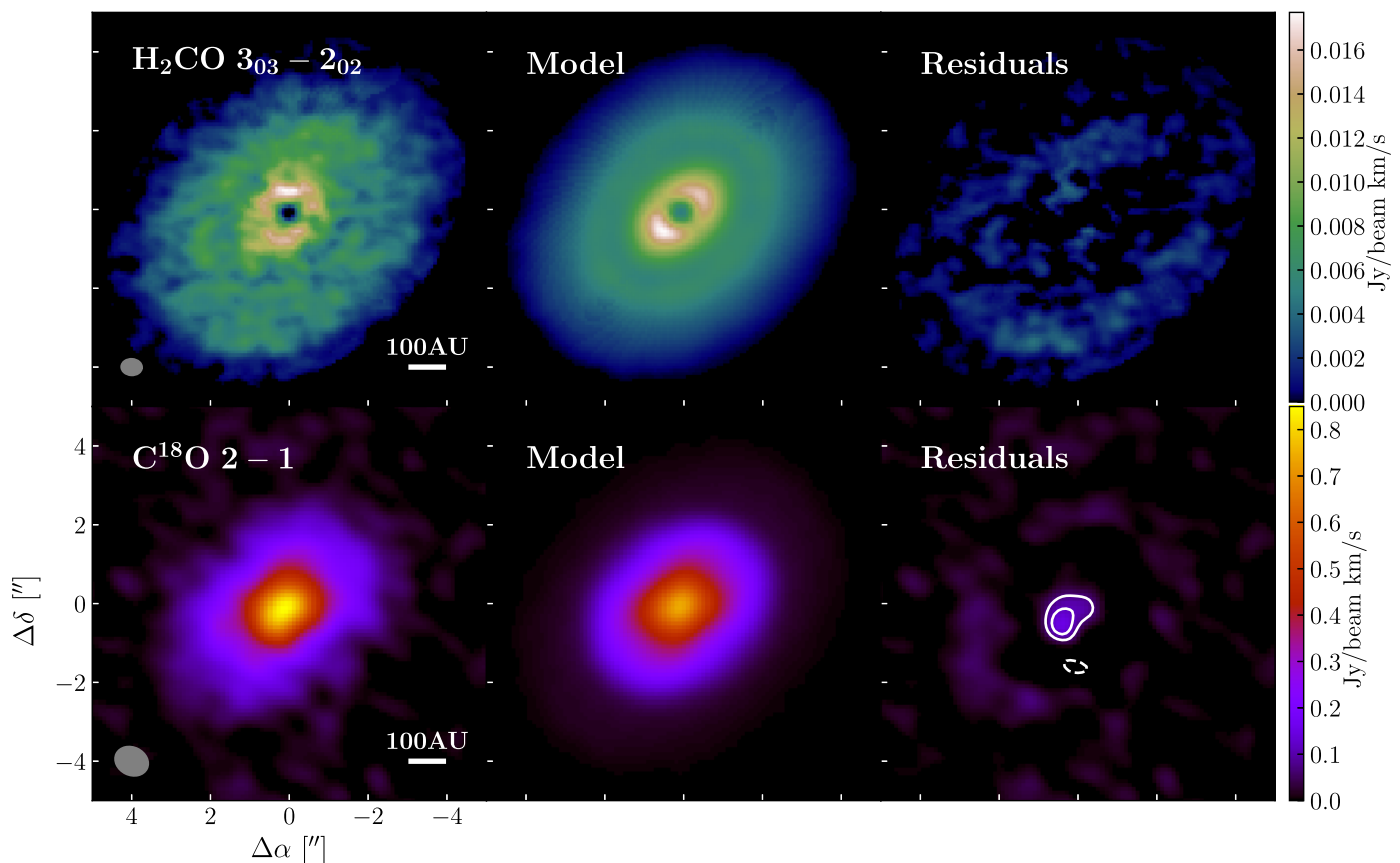


Fig. 8: Data, model, and residual integrated intensity maps. H₂CO 3₀₃–2₀₂ data and model maps are created after applying a Keplerian mask to the image cube (see Section 3.1). *Left:* H₂CO 3₀₃–2₀₂ data integrated intensity map from 0.76 – 10.84 km s^{–1} and C¹⁸O 2–1 data integrated intensity map from –0.88 – 12.48 km s^{–1}. Synthesized beam and AU scale are shown in the lower corners. *Center:* Integrated intensity map of best-fit model taken over the same velocity channels as the left figure. *Right:* Residual image with contours at 3σ intervals. Dashed contours are negative, solid contours are positive.

by a factor of a few up to one order of magnitude in the outer regions beyond ~300 AU.

Walsh et al. (2014) created a series of increasingly complex T Tauri disk chemical evolution models that include grain-surface formation to estimate abundances of complex organic molecules (COMs) throughout the disk. Beginning with freeze-out and thermal desorption only, they go on to include non-thermal desorption, grain-surface chemistry, radiative reprocessing of ices, and reactive desorption in their full disk model. The vertical distribution of H₂CO included a large gas-phase reservoir above the midplane reaching peak fractional abundances relative to H₂ of ~10^{–8} and an ice reservoir beyond 10 AU with peak fractional abundances of ~10^{–4}. Beyond 50 AU, the radial column density of H₂CO in the Walsh et al. (2014) comprehensive disk model shows an increase by a factor of a few.

From these two examples it is clear that a modest outer disk enhancement of H₂CO cannot immediately reveal whether gas-phase or grain-surface production is the dominant formation route. Full chemical modeling of H₂CO production is required. In this section we discuss possible explanations for the H₂CO enhancement in the outer disk around HD 163296, its relation to the CO snow line and the millimeter continuum, and the implications for H₂CO formation.

4.1. H₂CO and the CO snow line

Previous SMA observations of H₂CO in the disk around HD 163296 showed ring-like formaldehyde emission outside the expected CO snow line (Qi et al. 2013). The authors suggested that a scenario with only grain-surface formation could be responsible for the observed distribution and the apparent lack of centrally peaked emission. The lower spatial resolution and SNR per channel of the SMA observations would preferentially place the H₂CO emitting region farther away from the central star since the emission at smaller radii is spread out over more velocity channels due to the shear in the Keplerian disk, thus resulting in a false ring-like structure. The ALMA results presented here show that H₂CO is not present in a ring, but rather emission is seen throughout most of the gaseous extent of the disk, with a central depletion in the inner ~50 AU.

Qi et al. (2015) presented new constraints on the CO snow line in HD 163296 based on observations of C¹⁸O and N₂H⁺. N₂H⁺ is readily destroyed by gas-phase CO, thus it is expected to be a reliable tracer of CO depletion. By refitting the location and degree of CO depletion, they found that a factor of 5 depletion in column density at 85–90 AU improved their best-fit models to the visibility data. They interpret this radius as the location of the CO snow line, corresponding to a CO freeze-out temperature of 25 K. The coincident of CO depletion and N₂H⁺ emission inner radius supports the claim that N₂H⁺ traces regions of CO freeze-out. Recent results by van’t Hoff et al. (2017) show that the N₂H⁺

emission can peak from ~ 5 –50 AU beyond the location of the CO snow line and that careful chemical modeling is necessary to properly interpret the location of CO freeze-out from N_2H^+ observations.

The data presented here show that H_2CO extends beyond the Qi et al. (2015) CO freeze-out radius, but with a peak at ~ 90 AU that coincides with the CO snow line. Öberg et al. (in press) presented H_2CO observations in the disk around TW Hya and find that grain-surface formation of H_2CO begins at temperatures where CO starts to spend even a short time on the grains, meaning that H_2CO can be produced – and the emission can peak – just inside of the CO snow line. Considering our ~ 50 AU resolution, the peak seen at ~ 90 AU may be the beginning of grain surface formation of H_2CO , likely with some contribution from the warmer, gas-phase formation pathway at the innermost radii.

Recent analysis of ALMA Cycle 0 data for H_2CO in DM Tau explored the relative contributions of gas-phase and grain-surface formation pathways (Loomis et al. 2015). Their chemical models required both formation via gas-phase reactions and hydrogenation of CO ice in the outer regions of the disk to reproduce the centrally peaked and outer disk emission. Our simple parameterized models do not include chemical processing, but the presence of H_2CO at radii beyond the expected CO snow line at 90 AU and where millimeter grains are present indicates that grain-surface formation is a partial contributor to the H_2CO reservoir in the disk around HD 163296. Unlike the DM Tau results, our data also suggests that there is an intrinsic link between the edge of the millimeter continuum and the production of H_2CO in HD 163296.

4.2. The H_2CO inner hole

A sharp drop in H_2CO emission within 50 AU is evident in the integrated intensity map (see Figure 8) and by the best-fit R_{in} of the H_2CO models. Optically thick dust may be responsible for the observed depletion, rather than a drop in H_2CO abundance. Photons emitted by H_2CO in the midplane of the disk can be absorbed by optically thick dust in the upper layers, causing the inner hole – after continuum subtraction – that is seen in the H_2CO integrated intensity map.

Zhang et al. (2016) model the HD 163296 continuum visibilities using a parameterized radial intensity distribution modulated by multiple sine waves. Their best-fit model shows that there is an increase in millimeter-wavelength intensity of $\sim 60\%$ in the innermost 50 AU of the disk, causing the millimeter continuum to become optically thick in this region. Zhang et al. (2016) produced simulated model images with a $0.035''$ beam, which clearly shows the strong central continuum emission. At the spatial resolution presented in this work, $0.5''$, the millimeter continuum appears smooth. Isella et al. (2016) presented $0.2''$ observations of the 1.3 millimeter continuum and three CO isotopologues. They show central depressions in the ^{13}CO and C^{18}O maps, and concluded that both the CO and the dust become optically thick within 50 AU, leading to large uncertainties in their surface densities.

Öberg et al. (in press) observe a similar central H_2CO depression well within the CO snow line in the disk around TW Hya. While they do not rule out dust opacity effects completely, they prefer to explain it as a real drop in abundance, as the central depression is not seen in higher frequency lines of H_2CO or CO isotopologues. Observations of additional, high frequency H_2CO lines in the HD 163296 disk would be needed to test this scenario. The ^{13}CO and C^{18}O central holes seen by Isella et al.

(2016) at high resolution already suggest dust opacity as an explanation for the central H_2CO depression in this disk.

4.3. H_2CO and the millimeter continuum edge

The millimeter grains in HD 163296 have decoupled from the gas and drifted radially inward. Millimeter emission in the outer disk is truncated at 270 AU while the bulk of the gas, based on ^{12}CO observations, extends to ~ 550 AU (de Gregorio-Monsalvo et al. 2013). The outer edge of millimeter emission corresponds to the 270 ± 20 AU change-over radius for H_2CO enhancement found by the best-fit radial step-abundance model. Grain growth and radial drift in the outer regions of the disk can result in a decrease of small, micron-sized grains beyond ~ 270 AU. With less shielding from external and protostellar radiation, penetrating UV photons in the outer regions may cause an increase in the H_2CO photodesorption directly off icy grain surfaces (Öberg et al. 2009; Huang et al. 2016). Increased UV radiation in a dust-depleted outer disk could also lead to CO photodissociation in the upper layers, opening a more efficient gas-phase route for H_2CO where hydrocarbon radicals and atomic oxygen are readily available.

Dust evolution models for HD 163296 by Facchini, et al. (subm.) show that for a low-turbulence environment, a temperature inversion can occur around 300 AU, causing a second CO desorption front in the outer disk (also suggested qualitatively by Cleeves 2016). In that case, an increase of both C^{18}O and H_2CO abundance in the outer disk would be expected, but our models found a CO depletion. It may be that there are competing effects occurring in the outer disk for CO. A temperature inversion and/or UV photodesorption beyond 300 AU can cause the release of grain-surface H_2CO and a fraction of CO ice back into the gas phase near the midplane, but CO photodissociation in the upper layers may dominate the C^{18}O surface density profile so that we ultimately see an outer disk depletion in C^{18}O , and an increase in H_2CO production.

5. Conclusions

In this work, multiple detections with ALMA of H_2CO 3–2 in the protoplanetary disk around HD 163296 were presented: one robust detection via imaging, H_2CO $3_{03}-2_{02}$, and two weaker detections via matched filter analysis, H_2CO $3_{22}-2_{21}$ and H_2CO $3_{21}-2_{20}$. The distribution of H_2CO relative to C^{18}O and the millimeter continuum was analyzed using various model abundance profiles to test possible H_2CO formation scenarios. The conclusions of this work are as follows:

- H_2CO in HD 163296 is observed out to ~ 550 AU, equal to the full radial extent of the gas disk as observed with CO. It does not have a ring-like morphology.
- The kinetic temperature of the observed H_2CO gas has a lower limit of >20 K, thus emission from these lines can originate from the cold molecular reservoir near the disk midplane.
- The best-fit radial step-abundance model to the H_2CO $3_{03}-2_{02}$ data suggests that H_2CO has an inner radius $R_{\text{in}} = 50$ AU, an outer disk abundance a factor of two higher than the inner disk ($X_1/X_2 = 0.5$), and a change-over radius of $R_c = 270 \pm 20$ AU. There is a mechanism causing increased H_2CO production in the outer disk beyond the millimeter grains. One explanation is desorption of H_2CO from icy grains by thermal desorption due to a temperature inversion or by UV

photodesorption where CO is frozen out. Alternatively, photodissociation of CO in the outer disk may increase the efficiency of the CH₃ + O gas-phase route to form H₂CO.

- Based on the C¹⁸O 2–1 models presented in this work, two scenarios reproduce the data well: step-abundance models with abundance boundaries based on temperature and radius, respectively. The best-fit models both indicate depleted CO in the outer disk based on the recovery of the C¹⁸O 2–1 surface density profile. Both models have a CO depletion factor of 10 in the outer disk. The depletion is likely a combination of CO freeze-out in the disk midplane and photodissociation of CO in the disk upper layers due to penetrating UV radiation.
- The best-fit abundance for the C¹⁸O radial step-abundance model was $X_1 = 4–12 \times 10^{-8}$, $X_2 = 4–12 \times 10^{-9}$. The best-fit abundance for the H₂CO radial step-abundance model was $X_1 = 2–5 \times 10^{-12}$, $X_2 = 4–10 \times 10^{-12}$.

Further observations of HD 163296 can unambiguously determine the dominant formation pathway of H₂CO in the disk. Constraining the ortho- to para- ratio of the two H₂CO isomers can distinguish between grain surface formation and gas-phase formation (Guzmán et al. 2011). The H₂CO o/p ratio is expected to be less than three for grain-surface formation (Dulieu 2011; Fillion et al. 2012). Observations of co-spatial H₂CO and CH₃OH would also constrain the contributions of gas- and solid-phase H₂CO, as CH₃OH forms similarly via hydrogenation of CO ices and has no known gas-phase formation route.

Acknowledgements. The authors thank the referee for insightful comments and constructive suggestions. M.T.C. thanks S. Facchini and G.S. Mathews for useful discussion on dust evolution and CO chemistry in HD 163296. The authors acknowledge support by Allegro, the European ALMA Regional Center node in The Netherlands, and expert advice from Luke Maud in particular. This paper makes use of the following ALMA data: ADS/JAO.ALMA# 2013.1.01268.S and 2011.1.00010.SV. ALMA is a partnership of ESO (representing its member states), NSF (USA) and NINS (Japan), together with NRC (Canada), NSC and ASIAA (Taiwan), and KASI (Republic of Korea), in cooperation with the Republic of Chile. The Joint ALMA Observatory is operated by ESO, AUI/NRAO and NAOJ.

References

Aikawa, Y. & Herbst, E. 1999, *A&A*, 351, 233
 Aikawa, Y., Momose, M., Thi, W.-F., et al. 2003, *PASJ*, 55, 11
 Andrews, S. M. & Williams, J. P. 2005, *ApJ*, 631, 1134
 Atkinson, R., Baulch, D. L., Cox, R. A., et al. 2006, *Atmospheric Chemistry & Physics*, 6, 3625
 Brinch, C. & Hogerheijde, M. R. 2010, *A&A*, 523, A25
 Cleaves, L. I. 2016, *ApJ*, 816, L21
 Cuppen, H. M., van Dishoeck, E. F., Herbst, E., & Tielens, A. G. G. M. 2009, *A&A*, 508, 275
 D’Alessio, P., Calvet, N., Hartmann, L., Franco-Hernández, R., & Servín, H. 2006, *ApJ*, 638, 314
 de Gregorio-Monsalvo, I., Ménard, F., Dent, W., et al. 2013, *A&A*, 557, A133
 Dulieu, F. 2011, in *IAU Symposium*, Vol. 280, *The Molecular Universe*, ed. J. Cernicharo & R. Bachiller, 405–415
 Dullemond, C. P. & Dominik, C. 2005, *A&A*, 434, 971
 Fillion, J.-H., Bertin, M., Lekic, A., et al. 2012, in *EAS Publications Series*, Vol. 58, *EAS Publications Series*, ed. C. Stehlé, C. Joblin, & L. d’Hendecourt, 307–314
 Fockenberg, C. & Preses, J. M. 2002, *Journal of Physical Chemistry A*, 106, 2924
 Guzmán, V., Pety, J., Goicoechea, J. R., Gerin, M., & Roueff, E. 2011, *A&A*, 534, A49
 Herbst, E. & van Dishoeck, E. F. 2009, *ARA&A*, 47, 427
 Huang, J., Öberg, K. I., & Andrews, S. M. 2016, *ApJ*, 823, L18
 Isella, A., Guidi, G., Testi, L., et al. 2016, *Phys. Rev. Lett.*, 117, 251101
 Isella, A., Testi, L., Natta, A., et al. 2007, *A&A*, 469, 213
 Loomis, R. A., Cleaves, L. I., Öberg, K. I., Guzman, V. V., & Andrews, S. M. 2015, *ApJ*, 809, L25

Mathews, G. S., Klaassen, P. D., Juhász, A., et al. 2013, *A&A*, 557, A132
 McMullin, J. P., Waters, B., Schiebel, D., Young, W., & Golap, K. 2007, in *Astronomical Society of the Pacific Conference Series*, Vol. 376, *Astronomical Data Analysis Software and Systems XVI*, ed. R. A. Shaw, F. Hill, & D. J. Bell, 127
 Müller, H. S. P., Schlöder, F., Stutzki, J., & Winnewisser, G. 2005, *Journal of Molecular Structure*, 742, 215
 Mumma, M. J. & Charnley, S. B. 2011, *ARA&A*, 49, 471
 Öberg, K. I., Bottinelli, S., Jørgensen, J. K., & van Dishoeck, E. F. 2010a, *ApJ*, 716, 825
 Öberg, K. I., Garrod, R. T., van Dishoeck, E. F., & Linnartz, H. 2009, *A&A*, 504, 891
 Öberg, K. I., Qi, C., Fogel, J. K. J., et al. 2010b, *ApJ*, 720, 480
 Qi, C., D’Alessio, P., Öberg, K. I., et al. 2011, *ApJ*, 740, 84
 Qi, C., Öberg, K. I., Andrews, S. M., et al. 2015, *ApJ*, 813, 128
 Qi, C., Öberg, K. I., & Wilner, D. J. 2013, *ApJ*, 765, 34
 Rosenfeld, K. A., Andrews, S. M., Hughes, A. M., Wilner, D. J., & Qi, C. 2013, *ApJ*, 774, 16
 Sault, R. J., Teuben, P. J., & Wright, M. C. H. 1995, in *Astronomical Society of the Pacific Conference Series*, Vol. 77, *Astronomical Data Analysis Software and Systems IV*, ed. R. A. Shaw, H. E. Payne, & J. J. E. Hayes, 433
 Schoeier, F. L., van der Tak, F. F. S., van Dishoeck, E. F., & Black, J. H. 2005, *VizieR Online Data Catalog*, 343
 van den Ancker, M. E., de Winter, D., & Tjin A Djie, H. R. E. 1998, *A&A*, 330, 145
 van der Marel, N., van Dishoeck, E. F., Bruderer, S., & van Kempen, T. A. 2014, *A&A*, 563, A113
 van Dishoeck, E. F. & Blake, G. A. 1998, *ARA&A*, 36, 317
 van’t Hoff, M. L. R., Walsh, C., Kama, M., Facchini, S., & van Dishoeck, E. F. 2017, *A&A*, 599, A101
 Walsh, C., Millar, T. J., Nomura, H., et al. 2014, *A&A*, 563, A33
 Watanabe, N., Shiraki, T., & Kouchi, A. 2003, *ApJ*, 588, L121
 Wiesenfeld, L. & Faure, A. 2013, *MNRAS*, 432, 2573
 Yen, H.-W., Koch, P. M., Liu, H. B., et al. 2016, *ArXiv e-prints*
 Zhang, K., Bergin, E. A., Blake, G. A., et al. 2016, *ApJ*, 818, L16

Appendix A: Channel Maps

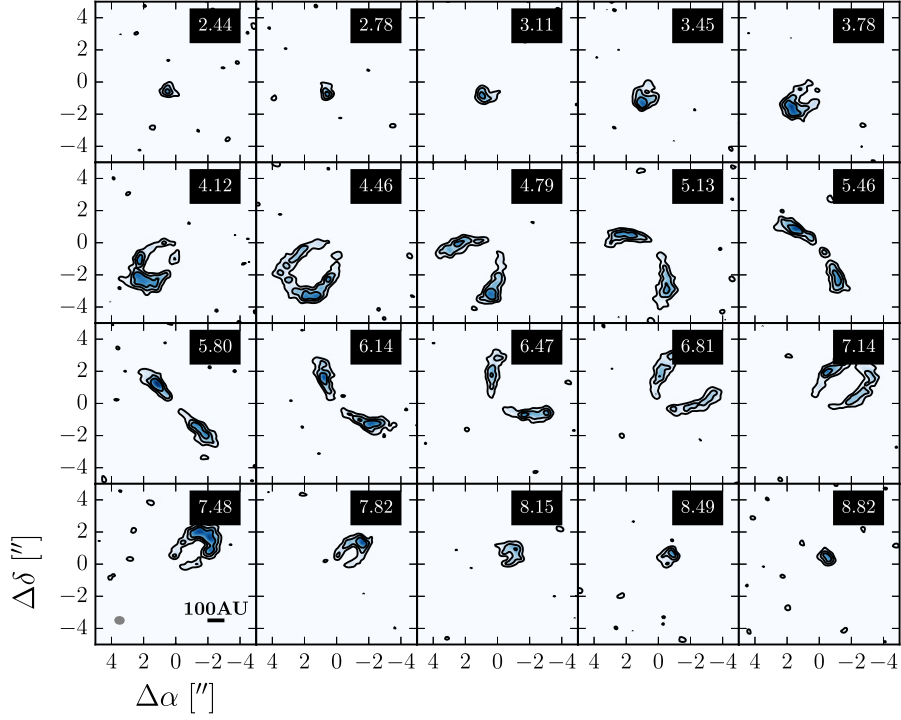


Fig. A.1: $\text{H}_2\text{CO } 3_{03}-2_{02}$ data channel maps, Hanning smoothed to 0.336 km s^{-1} channels. Black contours mark $1.5 \times 10^{-3} (1\sigma) \times [3, 6, 9] \text{ Jy beam}^{-1}$. Synthesized beam and AU scale are shown in the lower left panel.

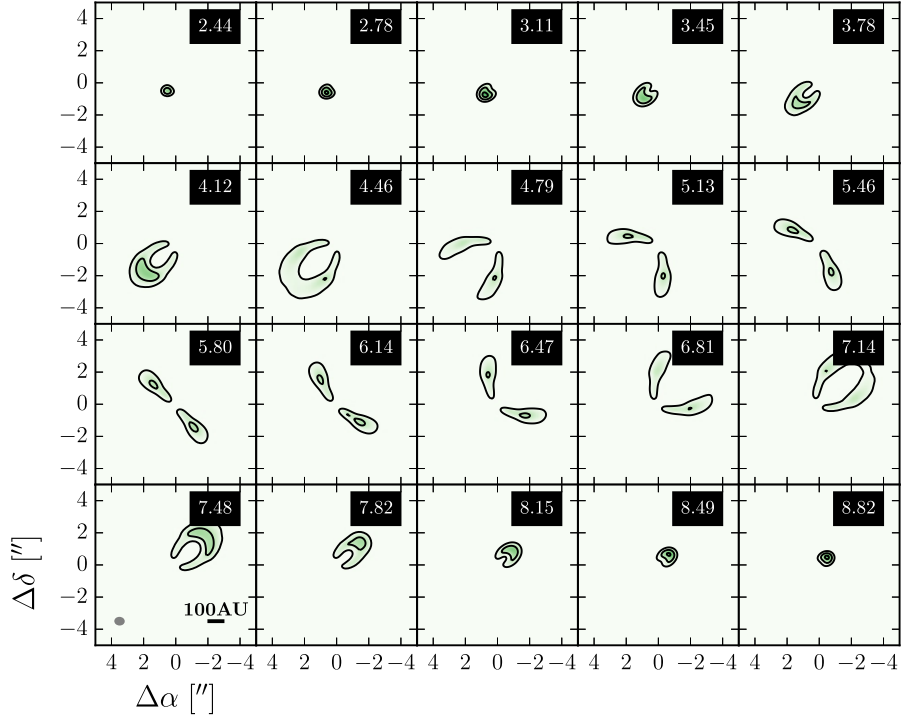


Fig. A.2: $\text{H}_2\text{CO } 3_{03}-2_{02}$ best-fit model channel maps, Hanning smoothed to 0.336 km s^{-1} channels. Black contours mark $1.5 \times 10^{-3} (1\sigma) \times [3, 6, 9] \text{ Jy beam}^{-1}$. Synthesized beam and AU scale are shown in the lower left panel.

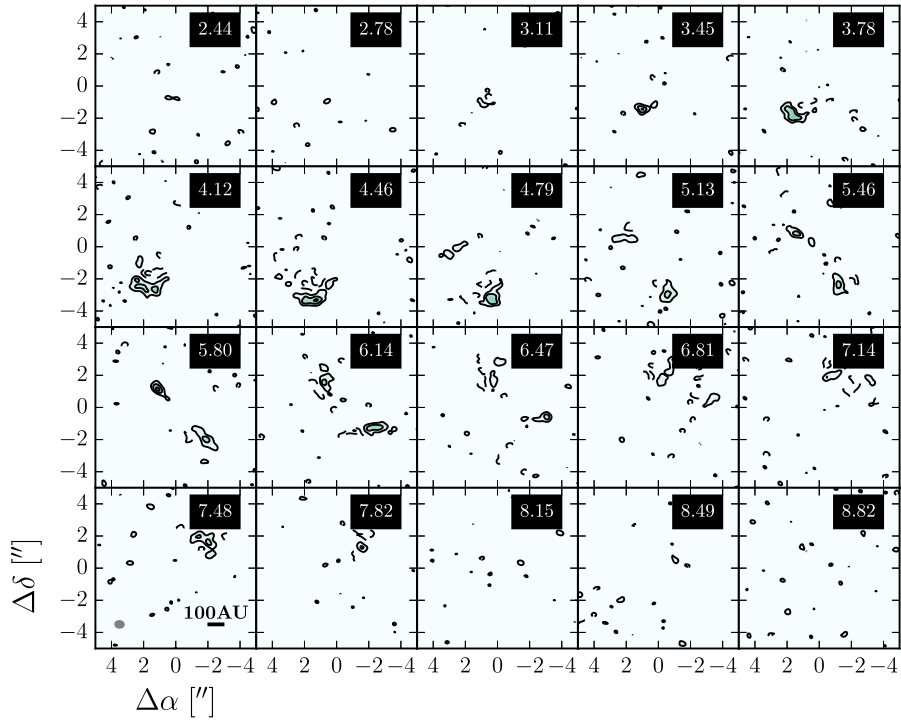


Fig. A.3: H₂CO 3₀₃–2₀₂ residual (data–model) channel maps, Hanning smoothed to 0.336 km s^{–1} channels. Black contours mark 1.5×10^{-3} (1σ) \times [3, 6, 9] Jy beam^{–1}. Dashed contours are negative at the same intervals. Synthesized beam and AU scale are shown in the lower left panel.

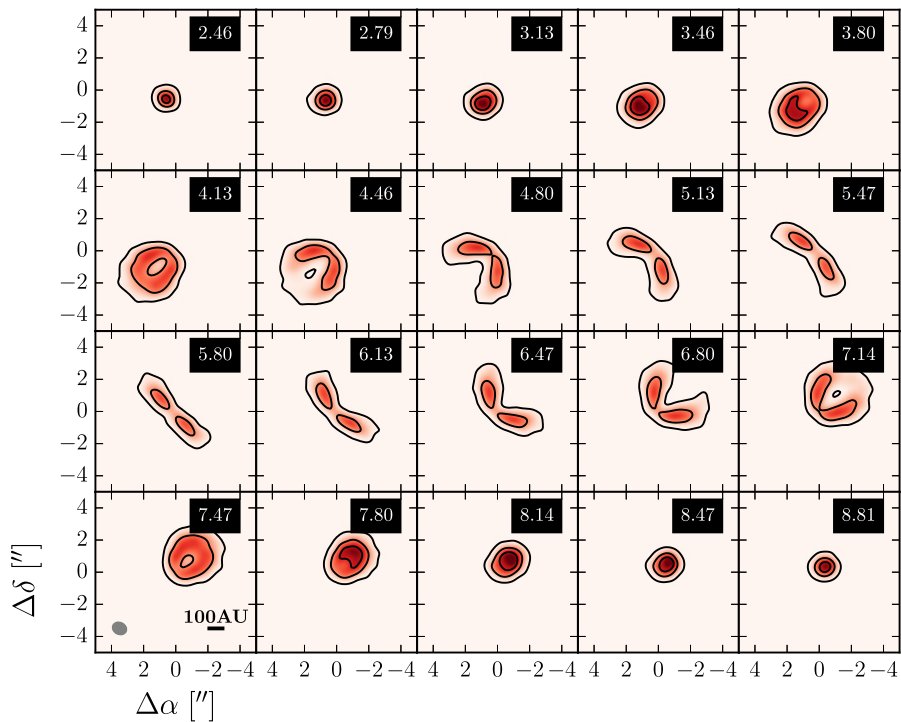


Fig. A.4: C¹⁸O 2–1 data channel maps. Black contours mark 4.2×10^{-3} (1σ) \times [5, 25, 45] Jy beam^{–1}. Synthesized beam and AU scale are shown in the lower left panel.

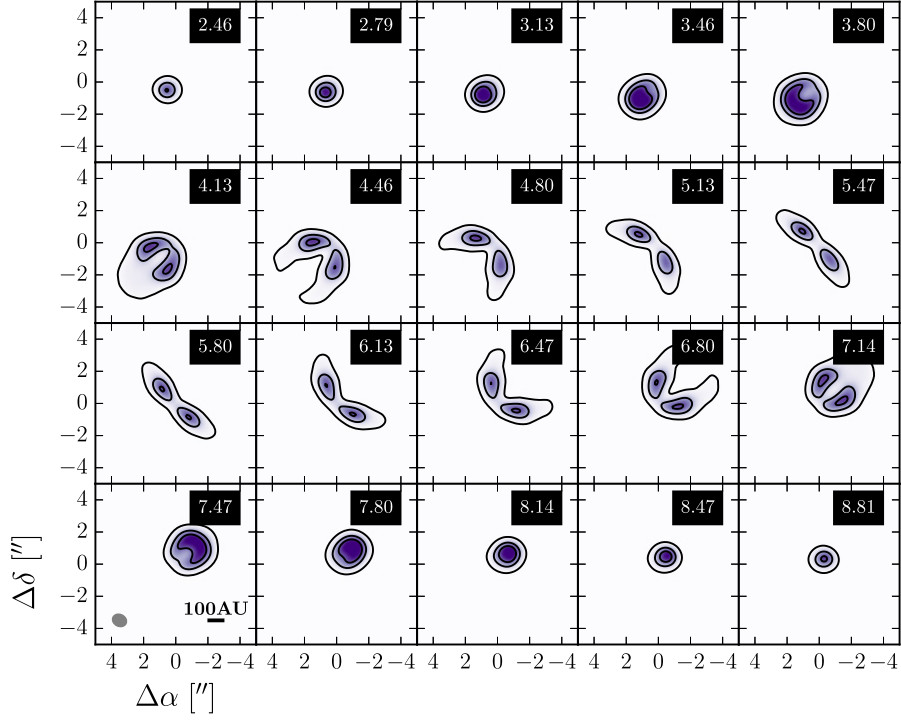


Fig. A.5: C^{18}O 2–1 best-fit model channel maps. Black contours mark $4.2 \times 10^{-3} (1\sigma) \times [5, 25, 45]$ Jy beam^{-1} . Synthesized beam and AU scale are shown in the lower left panel.

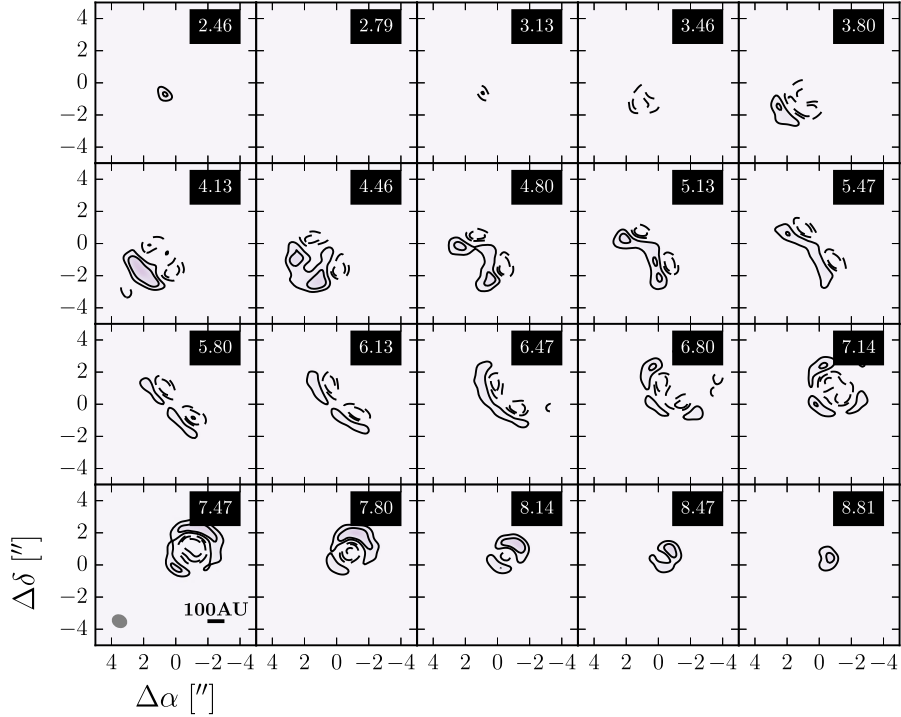


Fig. A.6: C^{18}O 2–1 residual (data–model) channel maps. Black contours mark $4.2 \times 10^{-3} (1\sigma) \times [5, 10, 20]$ Jy beam^{-1} . Dashed contours are negative at the same intervals. Synthesized beam and AU scale are shown in the lower left panel.